Supporting Information for

A Bioinspired Self-Balancing Magnetic Tactile Sensor for Intelligent Underwater Manipulation in the Deep Sea

Author Information

Naijia Xu[1,2], Daohui Zhang[1*], Qingyang Zheng[4], Xin Fu[1,2], Liyan Mo[5], Yuqi Qiao[1,2], Yunlong Dong[8], Xudong Hou[1,2], Lei Fu[8], Shuheng Ren[1,2], Yalun Gu[1,2], Zekai Wu[1,2], Shuaibing Liu[1,2], Qirui Su[1,2], Kaiwen Ping[1,2], Yaqi Chu[1], Dezhen Xiong[1], Qifeng Zhang[1], Yuangui Tang[1], Yunfei Bai[1], Yuwang Liu[1], Yiwen Zhao[1], Guorui Li[7], Huichan Zhao[6], Hao Wu[4], Tiefeng Li[3*], Lianqing Liu[1*], Xingang Zhao[1*].

1. State Key Laboratory of Robotics and Intelligent Systems, Shenyang Institute of Automation, Chinese Academy of Sciences, Shenyang 110016, China.

2. University of Chinese Academy of Sciences, Beijing 100049, China.

3. Center for X-Mechanics, Department of Engineering Mechanics, Zhejiang University, State Key Laboratory of Fluid Power and Mechatronic Systems, Institute of Fundamental and Transdisciplinary Research, Zhejiang University, Hangzhou, China.

4. Flexible Electronics Research Center, State Key Laboratory of Intelligent Manufacturing Equipment and Technology, School of Mechanical Science and Engineering, Huazhong University of Science and Technology, Hubei, Wuhan 430074, China.

5. Shien-Ming Wu School of Intelligent Engineering, South China University of Technology, Guangzhou 511442, China.

6. Department of Mechanical Engineering Tsinghua University, Beijing 100084, China.

7. College of Shipbuilding Engineering, Harbin Engineering University, Harbin,150001, China.

8. University of Shenyang University of Technology, Shenyang 110016, China.

*Corresponding author. Email: zhaoxingang@sia.cn(X.Z.);
liulianqing@sia.cn(L.L.);
litiefeng@zju.edu.cn(T.L.);
zhangdaohui@sia.cn(D.Z.).

Table of Contents

Supplementary Notes

Notes S1. Theoretical modeling of ciliary layer.

Note S2. Analytical Derivation of the Equivalent Stiffness for the Butterfly Porous Structure.

Note S3. Theoretical Modeling of Equivalent Contact Force and Magnetic Response Mechanism.

Supplementary Figures

Figure S1. Geometric dimensions of the unit cell of the butterfly-like porous structure for the deep-sea tactile sensor.

Figure S2. Schematic illustration of the fabrication process for the deep-sea tactile sensor.

Figure S3. Experimental platform for dynamic performance testing of the tactile sensor under high hydrostatic pressure.

Figure S4. Schematic of the small-scale laboratory hydrostatic pressure chamber.

Figure S5. Schematic showing the mechanical testing specimens and the corresponding experimental setup used in this study.

Figure S6. A set of objects used for testing the measurement range of the tactile sensor, featuring masses of 0.63 g (a feather), 18.9 L (drinking water), and 2 L (liquid for computers).

Figure S7. Validation of closed-loop control and non-damaging grasping based on tactile feedback.

Figure S8. Four material samples with different hardness levels used for gripping identification.

Figure S9. Schematic of the experiment for object hardness identification using the tactile sensor.

Figure S10. Hierarchical control architecture of the deep-sea tactile soft grasping system.

Figure S11. In-situ sea trial validation of the deep-sea tactile perception system deployed on the “Haidou-1” ROV.

Figure S12. Operational workflow of the deep-sea adaptive grasping system deployed on the ROV platform.

Figure S13. Time sequence diagram of 25-channel tactile forces during the sea star grasping process.

Figure S14. Time sequence diagram of 25-channel tactile forces during the sea cucumber grasping process.

Figure S15. Time sequence diagram of 25-channel tactile forces during the sea snail grasping process.

Figure S16. Time sequence diagram of 25-channel contact forces during the tactile-feedback-based collaborative sampling process.

Supplementary Tables

Table S1. Parameter table of butterfly structure.

Table S2. Geometric dimensions of the structure.

Table S3. Performance parameters of existing underwater tactile sensors.

Other Supplementary Material for this manuscript includes the following:

Movie S1(.mp4 format). Demonstration of the sensor's wide dynamic range and high resolution from millinewton-scale to large-scale loads.

Movie S2(.mp4 format). Impact resistance test and rapid signal recovery under high-energy collision.

Movie S3(.mp4 format). Non-destructive grasping of diverse underwater targets using tactile feedback closed-loop control.

Movie S4(.mp4 format). Stiffness discrimination and signal stability under 60 MPa hydrostatic pressure.

Movie S5(.mp4 format). Dynamic tactile mapping and contour reconstruction of an underwater target.

Notes S1. Theoretical modeling of ciliary layer

S1-1. Mechanical modeling of individual cilium

The ciliary layer consists of an array of magnetic composite microstructures. Each cilium is modeled as a cantilever beam based on the Euler–Bernoulli beam theory, which is applicable under the assumptions of small deformations, linear elastic material behavior, and negligible shear deformation.

For a cilium with a cylindrical cross-section of diameter D, the second moment of inertia I is given by:

$$I = \frac{\pi D^4}{64} \tag{1}$$

Where D is the diameter of the cilium.

Under a point load F applied at the free end, the deflection H at that end is expressed as:

$$H = \frac{Fl^3}{3EI} \tag{2}$$

Where l is the length of the cilium and E is the Young's modulus of the magnetic composite material.

S1-2. Equivalent stiffness of the ciliary layer

The equivalent stiffness K_c of a single cilium, defined as the ratio of the applied force to the resulting tip displacement, follows from Equation (2):

$$K_{\mathrm{c}} = \frac{F}{H} = \frac{3EI}{l^3} \tag{3}$$

To characterize the collective mechanical response of the ciliary array, we define an equivalent areal stiffness K_{layer} as the stiffness per unit projected area. Assuming a uniform array with n cilia per unit area, and neglecting interactions between cilia under small static deflection, the total force per unit area for a given uniform tip displacement H is $n \times F$. Therefore,

$$K_{\mathrm{layer}} = nK_c = \frac{3nEI}{L^3} \tag{4}$$

This parameter K_{layer} (units: N/m^3) represents the effective elastic modulus of the ciliary layer when treated as a continuum in subsequent analysis.

Note S2. Analytical Derivation of the Equivalent Stiffness for the Butterfly Porous Structure

S2-1 Geometric Parameterization of the Unit Cell

To simplify the calculations and exploit the structural symmetry, we established a quarter-unit-cell model of the butterfly-like porous structure for analysis (**Fig. S1**). Boundary conditions were applied in accordance with the planes of symmetry: point A at the intersection of the symmetry planes was fully fixed, while points D and E on the symmetry planes were constrained against rotation about the z-axis. A concentrated force F was applied along the y-direction at the relevant nodes to simulate the uniaxial compressive loading experienced by the unit cell under realistic contact conditions. This simplified model not only captures the global mechanical behavior effectively but also significantly enhances computational efficiency.

S2-2 Force Method for Solving the Statically Indeterminate Structure

The quarter-unit-cell model is a doubly statically indeterminate structure. To determine its internal forces, we analyzed it using the Force Method. Two key bending moments were selected as the redundant forces, denoted as X_1 and X_2. Following the principle of the Force Method, canonical equations were established by enforcing deformation compatibility conditions at these two sections:

$$\begin{cases} \delta_{11}X_1 + \delta_{12}X_2 + \Delta_{1p} = 0 \\ \delta_{21}X_1 + \delta_{22}X_2 + \Delta_{2p} = 0 \end{cases} \tag{5}$$

Here, δ_{ij} denotes the displacement coefficient along the X_i direction induced by a unit unknown force $X_j = 1$, while Δ_{ip} represents the displacement along the X_i direction caused solely by the external load F. This set of equations fully describes the deformation compatibility of the structure and forms the basis for solving the statically indeterminate internal forces.

By solving the canonical equations of the Force Method, the analytical solutions for the unknown bending moments at the two critical sections are obtained:

$$\begin{aligned} M_1 = X_1 &= \frac{F\left[l_1\left(A_{10}\sin\alpha + A_3\sin\beta + l_3^2\sin\gamma\right)\right]}{2A_1} \\ M_2 = X_2 &= \frac{F\left[l_1\sin\alpha\left(A_2 + 2A_4\right) - l_4\left(A_3\sin\beta + l_3^2\sin\gamma\right)\right]}{2A_1} \end{aligned} \tag{6}$$

In Equation (6), the coefficients A_1, A_2, A_3, A_4, A_{10} are related to the structural geometric dimensions, and their specific expressions are listed in **Table S1**. This result clarifies the quantitative relationship between the sectional bending moment, the applied load, and the geometric parameters, providing a basis for subsequent internal force and equivalent performance analysis.

S2-3 Method of Superposition for Displacement Calculation

Displacement calculation was performed using the method of superposition. This method involves calculating the deformation of each major structural member (including CE, CB, AB, and CD) under the external load separately to determine its displacement component in the y-direction. The total displacement of the entire quarter-unit-cell in the direction of the applied load is then obtained by linear superposition. Based on the assumptions of small deformation and linear elasticity, this approach decomposes the displacement analysis of a complex structure into the sequential calculation and synthesis of individual member deformations, thereby systematically and clearly revealing the quantitative relationship between the load and the overall deformation.

S2-3.1 Displacement of Member CE

The displacement of member CE in the y-direction was calculated using the method of superposition. This displacement is the sum of three superimposed contributions: the bending displacement δ_{CEy}^{M} due to moment, the axial displacement $\delta_{CEy}^{\mathrm{N}}$ due to axial force, and the shear displacement $\delta_{CEy}^{\mathrm{S}}$ due to shear force. Each component is calculated as follows.

The bending displacement, caused by the sectional bending moment, is expressed as:

$$\begin{aligned}\delta_{CEy}^{M} = \frac{F\sin^2\alpha}{2Est^3A_1^3}\{&\left[l_1A_2 + l_4\csc\alpha\left(A_3\sin\beta + l_3^2\sin\gamma\right)\right]^3 \\ &-\left[l_4\csc\alpha\left(A_3\sin\beta + l_3^2\sin\gamma\right) - l_1\left(A_2 + 2A_4\right)\right]^3\}\end{aligned} \tag{7}$$

The axial displacement due to the axial force is expressed as:

$$\delta_{CEy}^{\mathrm{N}} = \frac{Fl_1}{Est}\cos^2\alpha \tag{8}$$

The shear displacement, induced by the shear force and accounting for the shear shape factor, is expressed as:

$$\delta_{CEy}^{\mathrm{S}} = \frac{12(1+\mu_0)Fl_1}{5Est}\sin^2\alpha \tag{9}$$

The total displacement of member CE in the y-direction is given by the sum of the aforementioned three displacement components:

$$\delta_{CEy} = \delta_{CEy}^{M} + \delta_{CEy}^{N} + \delta_{CEy}^{S} \tag{10}$$

In Equations (7), (8), and (9), E represents the material's elastic modulus, u_0 denotes the Poisson's ratio, and the remaining coefficients are detailed in **Table S1** and **Table S2**. This formulation systematically describes the deformation composition

of the structural member, providing the necessary foundation for the subsequent synthesis of the overall displacement.

S2-3.2 Displacement of Member CB

The same method of superposition as that used for member CE was employed to calculate the displacement of member CB in the y-direction. This displacement similarly comprises three superimposed components: those induced by bending moment, axial force, and shear force.

The bending displacement, induced by the bending moment, is expressed as:

$$\delta_{CBy}^{M}=\frac{F\sin^{2}\beta}{2E_{0}st^{3}A_{1}^{3}}\begin{Bmatrix}\left[A_{5}-\csc\beta\left(A_{8}+A_{6}\sin\gamma\right)\right]^{3}\\+\left[A_{3}\left(l_{1}+l_{4}\right)+\csc\beta\left(A_{8}+A_{6}\sin\gamma\right)\right]^{3}\end{Bmatrix} \tag{11}$$

The axial compressive displacement induced by the axial force is expressed as:

$$\delta_{CBy}^{N}=\frac{Fl_{2}}{E_{0}st}\cos^{2}\beta \tag{12}$$

The shear displacement, induced by the shear force and considering the shear shape factor, is expressed as:

$$\delta_{CBy}^{S}=\frac{12(1+\mu_{0})Fl_{2}}{5E_{0}st}\sin^{2}\beta \tag{13}$$

Therefore, the total displacement of member CB in the y-direction is given by:

$$\delta_{CBy}=\delta_{CBy}^{M}+\delta_{CBy}^{N}+\delta_{CBy}^{S} \tag{14}$$

S2-3.3 Displacement of Member AB

The bending displacement, induced by the bending moment, is expressed as:

$$\delta_{ABy}^{M}=\frac{F\csc\gamma}{2E_{0}st^{3}A_{1}^{3}}\left[\left(A_{7}-A_{8}+A_{9}\sin\gamma\right)^{3}-\left(A_{7}-A_{8}-A_{6}\sin\gamma\right)^{3}\right] \tag{15}$$

The axial compressive displacement induced by the axial force is expressed as:

$$\delta_{ABy}^{N}=\frac{Fl_{3}}{E_{0}st}\cos^{2}\gamma \tag{16}$$

The shear displacement, induced by the shear force and considering the shear shape factor, is expressed as:

$$\delta_{ABy}^{S}=\frac{12(1+\mu_{0})Fl_{3}}{5E_{0}st}\sin^{2}\gamma \tag{17}$$

Therefore, the total displacement of member AB in the y-direction is given by:

$$\delta_{ABy}=\delta_{ABy}^{M}+\delta_{ABy}^{N}+\delta_{ABy}^{S} \tag{18}$$

S2-3.4 Displacement of Member CD

The bending displacement, induced by the bending moment, is expressed as:

$$\delta_{CDy}^{M}=\frac{3Fl_{4}^{2}}{E_{0}st^{3}A_{1}^{3}}\left(A_{10}\sin\alpha+A_{3}\sin\beta+l_{3}^{2}\sin\gamma\right)^{2} \tag{19}$$

The shear displacement, induced by the shear force and considering the shear shape factor, is expressed as:

$$\delta_{CDy}^{S} = \frac{12(1+\mu_0)Fl_4}{5E_0st} \tag{20}$$

Therefore, the total displacement of member CD in the y-direction is given by:

$$\delta_{CDy} = \delta_{CDy}^{M} + \delta_{CDy}^{S} \tag{21}$$

S2-3.5 Derivation of the Equivalent Stiffness

Based on the calculated displacement components for each member of the quarter-unit-cell obtained in Sections S2-3 using the method of superposition, the total displacement of the unit cell in the y-direction, denoted as δ_y, was derived using the principle of linear superposition. Its expression is as follows:

$$\delta_y = \delta_{CEy} + \delta_{CBy} + \delta_{ABy} + \delta_{CDy} \tag{22}$$

In the equation, δ_{CEy}, δ_{CBy}, δ_{ABy} and δ_{CDy} represent the total displacement in the y-direction for the corresponding members. The calculation comprehensively accounts for the contributions of bending moments, axial forces, and shear forces to the deformation. This total displacement characterizes the overall compressive deformation of the unit cell under the specified boundary and loading conditions.

Furthermore, based on the relationship between force and displacement, the equivalent stiffness K_y of the quarter-unit-cell in the y-direction can be derived. Since the analyzed model represents half of a symmetric structure (the quarter-unit-cell under symmetric boundary conditions), a conversion relationship exists between its overall stiffness and that of the half-structure. The specific expression is given by:

$$K_y = \frac{F}{2\delta_y} \tag{23}$$

Where F is the applied concentrated load. This equivalent stiffness reflects the macroscopic deformation resistance of the butterfly-like porous structure in the y-direction, providing a crucial theoretical foundation for the subsequent prediction of the material's equivalent elastic modulus and for structural optimization.

For a macroscopic structure composed of an array of porous butterfly-shaped unit cells, its overall stiffness can be derived from the individual cell stiffness and the arrangement of the array. Considering a rectangular array consisting of i rows and j columns of unit cells (denoted as an $i \times j$ array), a scaling relationship exists between the overall equivalent stiffness K_{array} and the stiffness of a single unit cell K_{unit}, expressed as follows:

$$K_{\text{array}} = \frac{j}{i} K_{\text{unit}} \tag{24}$$

The derivation of this relationship is based on a series-parallel mechanical model: Within each row, j unit cells are connected in parallel along the horizontal direction. These cells share identical displacement, and the resultant force on the row equals the sum of the forces on each cell. Therefore, the equivalent stiffness of a single row is $K_{\text{row}} = jK_{\text{unit}}$. In the vertical direction, the i rows are connected in series. Each row is subjected to the same external force, and the total displacement equals the sum of the displacements of all rows, meaning the overall compliance equals the sum of the compliances of each row, leading to the following expression:

$$\frac{1}{K_{\text{array}}} = \frac{i}{K_{\text{row}}} = \frac{i}{j} K_{\text{unit}} \tag{25}$$

Note S3. Theoretical Modeling of Equivalent Contact Force and Magnetic Response Mechanism

S3-1 Fundamental Theory of Magnetic Dipoles

The magnetic field B generated at an arbitrary observation point r in space by a magnetized component is given by the magnetic dipole field formula:

$$\mathrm{B(r)} = \frac{\mu_0}{4\pi}\left[\frac{3(\mathrm{m}\cdot\hat{\mathrm{a}})\hat{\mathrm{a}} - \mathrm{m}}{a^3}\right] \tag{26}$$

Where m is the magnetic dipole moment; $a = r - r'$ is the vector pointing from the dipole location r' to the observation point, with magnitude $a = |\mathrm{a}|$ and unit vector $\hat{\mathrm{a}} = \mathrm{a}/a$; and μ_0 is the vacuum permeability.

S3-2 Segmented Magnetic Field Response Mechanism

The layered structural design of this tactile sensor enables wide-range and high-sensitivity perception of external forces. In the micro-contact force stage, the low-modulus cilium layer dominates the deformation. Its significant bending displacement is efficiently converted into magnetic signal variation, thereby achieving high-sensitivity detection. When the external force increases further, the higher-modulus porous scaffold begins to undergo significant deformation and bears the main load. At this point, the system enters a stage of cooperative deformation dominated by the compression of the butterfly structure, supplemented by the elastic bending of the cilium. Consequently, the mechanical response and the resultant magnetic signal exhibit two characteristic stages: a high-sensitivity regime at low forces and a wide-load-bearing regime at high forces.

S3-2.1 Stage I: Cilium-Dominated Deformation

In this stage, the stiffness of the butterfly intermediate layer is very high, and its deformation is negligible. Only the cilium, acting as a fixed-base cantilever beam, undergoes elastic bending. Its deflection curve $w(z)$ and rotation angle $\theta(z)$ are:

$$\begin{aligned} w(z) &= \frac{F}{6E_{\mathrm{eq}}I}\left(3Lz^2 - z^3\right), \quad 0 \le z \le L \\ \theta(z) &= \frac{F}{2E_{\mathrm{eq}}I}\left(2Lz - z^2\right) \end{aligned} \tag{27}$$

The cilium deformation alters the spatial distribution of the magnetic dipole. The resulting change in the vertical magnetic field component $\Delta B_z^{(1)}$ at a fixed observation point is obtained by integrating the dipole field along the magnetized segment:

$$\Delta B_z^{(1)}(F) = \int_{z_1}^{z_2} \frac{\mu_0 MA}{4\pi} \cdot \frac{3\left[\hat{\mathrm{t}}(z)\cdot\mathrm{a}\right]a_z - a^2\cos\theta(z)}{a^5\cos\theta(z)}\,dz \tag{28}$$

Where $\hat{\mathrm{t}}(z)=\left(\sin\theta(z),0,\cos\theta(z)\right)$ is the tangent vector direction of the magnetic moment. Under the small deformation approximation, the response is linear:

$$\Delta B_z^{(1)} \propto F \tag{29}$$

S3-2.2 Stage II : Cooperative Deformation of Butterfly Layer and Cilium

When the external force exceeds the threshold, the butterfly intermediate layer produces significant displacement δ_y . Consequently, the base of the cilium undergoes a rigid-body displacement, with its elastic deformation superimposed on this displacement:

$$\begin{aligned} w(z) &= \delta_b + \frac{F}{6E_{\mathrm{eq}}I}\left(3Lz^2 - z^3\right)dz \\ \theta(z) &= \frac{F}{2E_{\mathrm{eq}}I}\left(2Lz - z^2\right) \end{aligned} \tag{30}$$

In this stage, the relative position vector a' to the observation point must account for both the elastic bending $w(z)$ and the base displacement δ_b:

$$\mathrm{a}' = \left(x_0 - w(z)\cos\varphi,\, y_0 - w(z)\sin\varphi,\, z_0 - z - \delta_b\right) \tag{31}$$

The corresponding change in the vertical magnetic field component $\Delta B_z^{(2)}$ is:

$$\Delta B_z^{(2)}(F) = \int_{z_1}^{z_2} \frac{\mu_0 MA}{4\pi} \cdot \frac{3\left[\hat{\mathrm{t}}(z)\cdot \mathrm{a}'\right]a'_z - (a')^2\cos\theta(z)}{(a')^5\cos\theta(z)}dz \tag{32}$$

S3-3 Integrated Response Function and Model Significance

Integrating the responses from both stages, the total change in the vertical magnetic field ΔB_z for the entire sensing unit is a piecewise function of the external force F:

$$\Delta B_z(F) = \begin{cases} \Delta B_z^{(1)}(F), & 0 \le F < F_{\mathrm{threshold}} \\ \Delta B_z^{(2)}(F), & F \ge F_{\mathrm{threshold}} \end{cases} \tag{33}$$

This magneto-mechanical coupling model fully reveals the physical mechanism underlying the transition from a micro-force linear response to a large-force nonlinear response. It establishes a quantitative theoretical relationship between the applied external force and the measurable magnetic field signal, providing the core theoretical basis for subsequent sensor design, and sensitivity optimization.

Table S1. Parameter table of butterfly structure

Parameters	Expressions
A_1	$l_1(l_1+l_3+l_4)+l_4(l_2+l_3))$
A_2	$l_1(l_2+l_3+l_4)$
A_3	$l_2(l_2+2l_3)$
A_4	$l_4(l_2+2l_3)$
A_5	$l_2[l_2l_4+l_1(l_2+2l_4)]$
A_6	$l_3^2(l_1+l_4)$
A_7	$l_2\sin\beta(l_1l_2+2l_1l_4+l_2l_4)$
A_8	$l_1^2l_4\sin\alpha$
A_9	$l_3[l_1(2l_2+l_3+2l_4)+l_4(2l_2+l_3)]$
A_{10}	$-l_1(l_2+l_3)$
B_1	$l_2[l_1(l_2-2l_3+4l_4)+l_4(l_2-2l_3)]$
B_2	$l_1l_2^2l_4\sin 2\beta$
B_3	$\frac{l_2}{2}\sin\beta(l_1+l_4)$
B_4	$l_3\sin\gamma[2l_4+l_1(l_2+l_4)]$
B_5	$l_2\sin\beta[2l_4+l_1(l_2+2l_4)]$
B_6	$l_3\sin\gamma[l_1(4l_2+l_3+4l_4)+l_4(4l_2+l_3)]$

Table S2 Geometric dimensions of the structure

length	mm	Angle	°
l_1	5.53	α	63
l_2	8.43	β	78
l_3	5.53	γ	63
l_4	0.815		
t	0.62		
s	15		

Table S3 Performance parameters of existing underwater tactile sensors

Refs.	Detection Range	Maximum Sensitivity	Response/recover time (ms)	Simulated Depth	Field-validated Depth
[1]	45-625kpa	$1.2kpa^{-1}$	150,N/A	100m	5m
[2]	8.9-94.6kpa	$0.77kpa^{-1}$	32,78	3000m	< 3m
[3]	0.062-450kpa	$0.0338kpa^{-1}$	100,400	< 1m	N/A
[4]	0-12N	$0.058N^{-1}$	200,250	50m	N/A
[5]	0-2N	$82.62N^{-1}$	30,30	5000m	N/A
[6]	50-600kpa	$0.62kpa^{-1}$	190,670	100m	N/A
[7]	0-30N	N/A（3N）	N/A	3000m	1384m
[8]	0-18kpa	<5pa	N/A	1.8m	1.6m
This work	**0.0063-718N**	**43.72 μT/N**	**12,24**	**12000m**	**2284.7m**

Note: The “N/A” denotes no relevant performance data

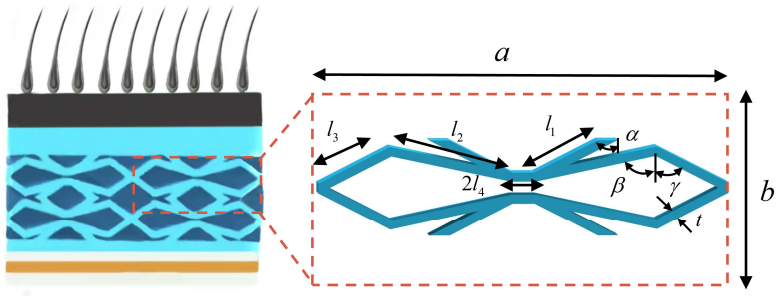

Figure S1. Geometric dimensions of the unit cell of the butterfly-like porous structure for the deep-sea tactile sensor.

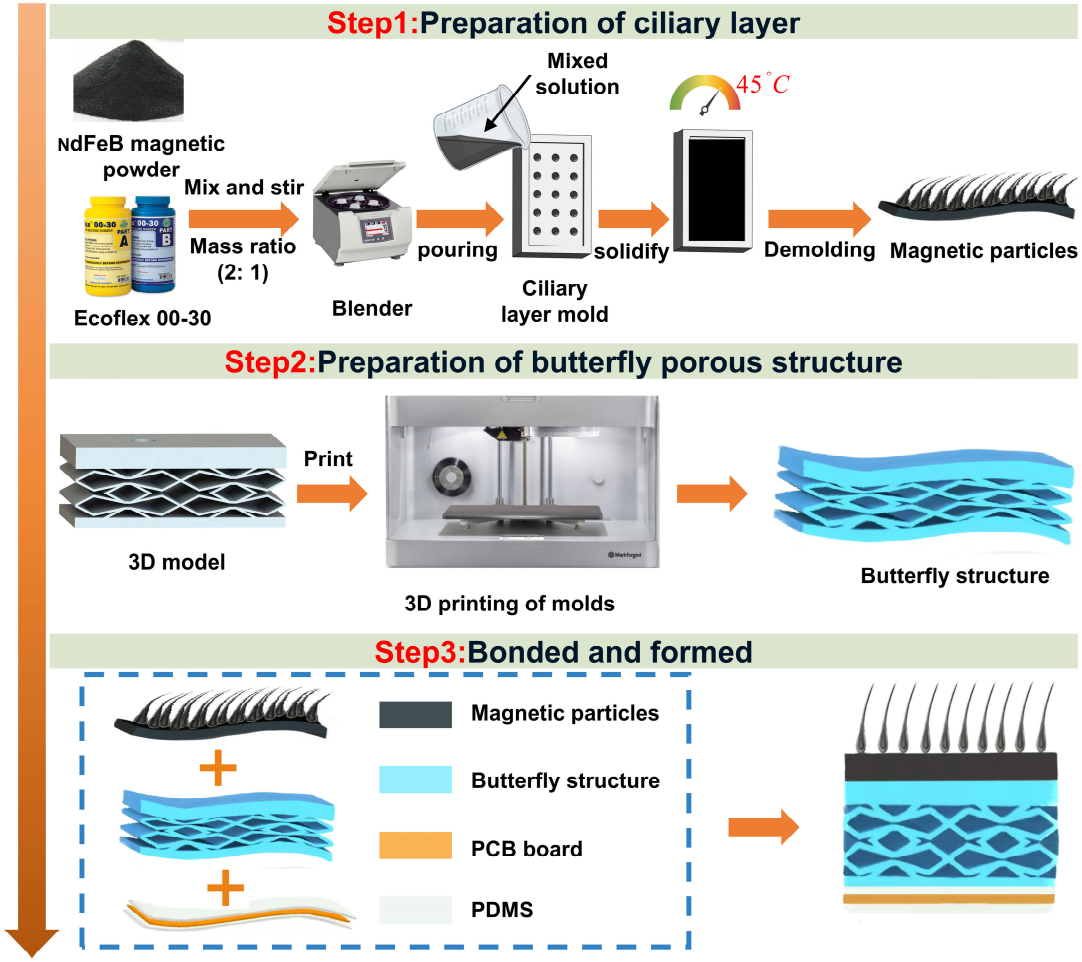

Figure S2. Schematic illustration of the fabrication process for the deep-sea tactile sensor. The device features a bio-inspired layered architecture designed to achieve both high sensitivity and a broad pressure-response range.

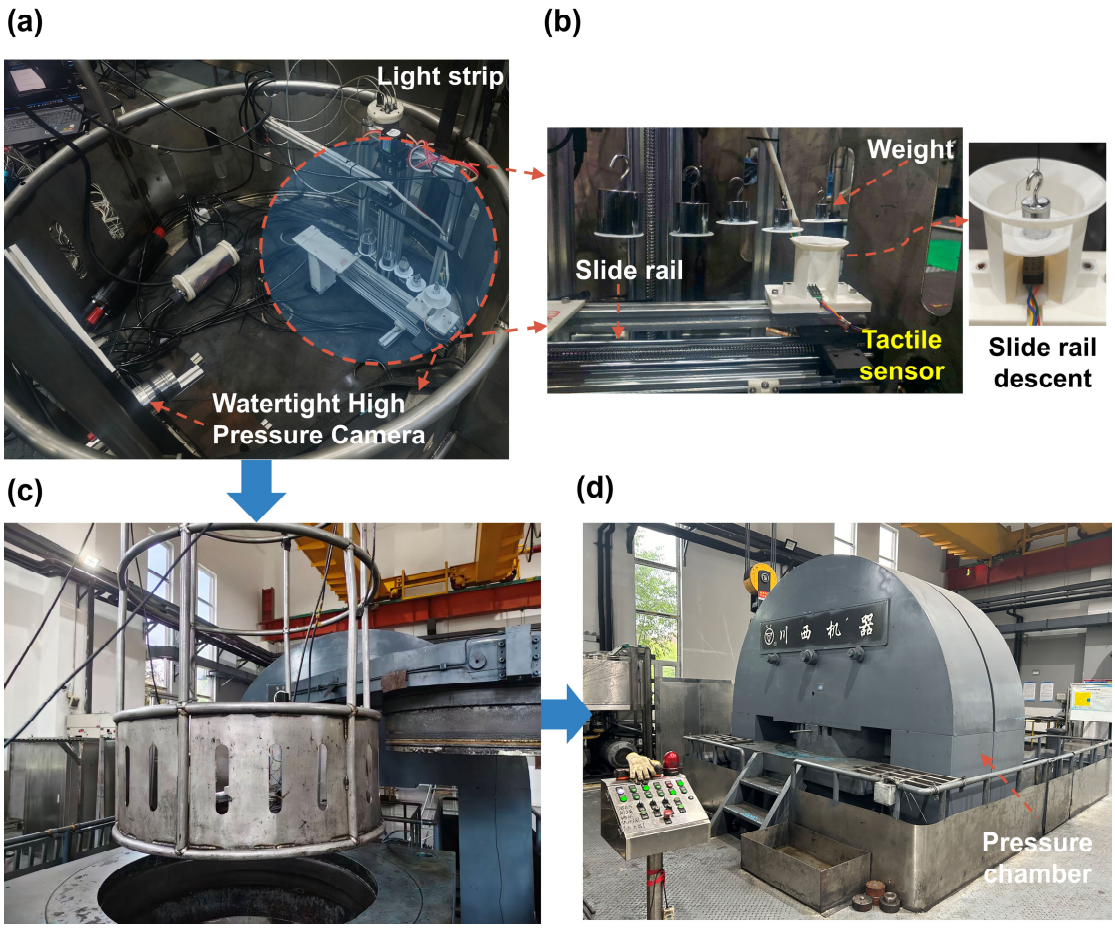

Figure S3. Experimental platform for dynamic performance testing of the tactile sensor under high hydrostatic pressure. (a) Schematic of sensor mounting and loading. The tactile sensor is fixed to a test base, and a standard weight, controlled via a precision sliding rail above it, is used to apply precisely calculable contact loads. (b) Close-up view of the weight loading motion. (c) Schematic illustrating the complete test platform positioned inside the high-pressure chamber. (d) Actual state of the fully integrated test system within the high-pressure chamber.

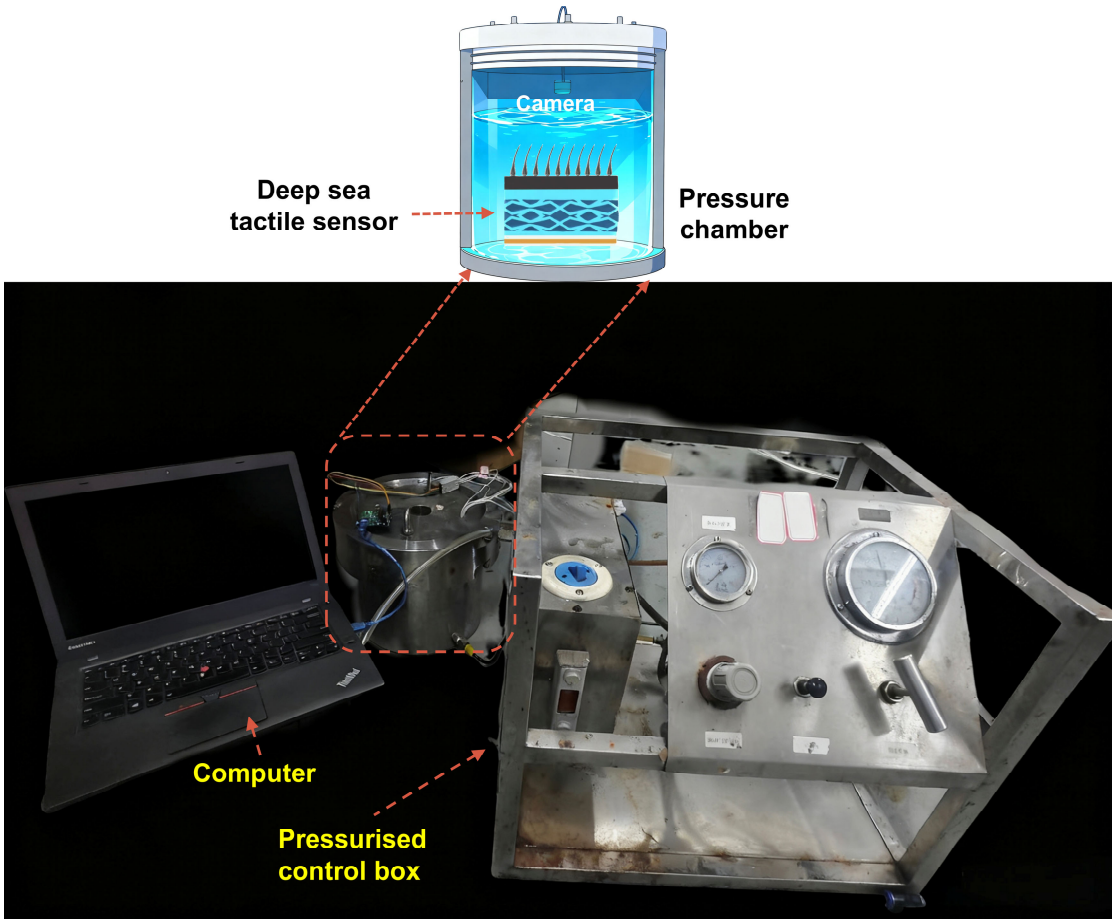

Figure S4. Schematic of the small-scale laboratory hydrostatic pressure chamber. The chamber has a maximum working pressure of 30 MPa, capable of simulating an environment equivalent to approximately 3000 meters water depth. The inset provides a detailed view of the bio-inspired tactile sensor's placement and its connection via waterproof cables to the external real-time signal acquisition system.

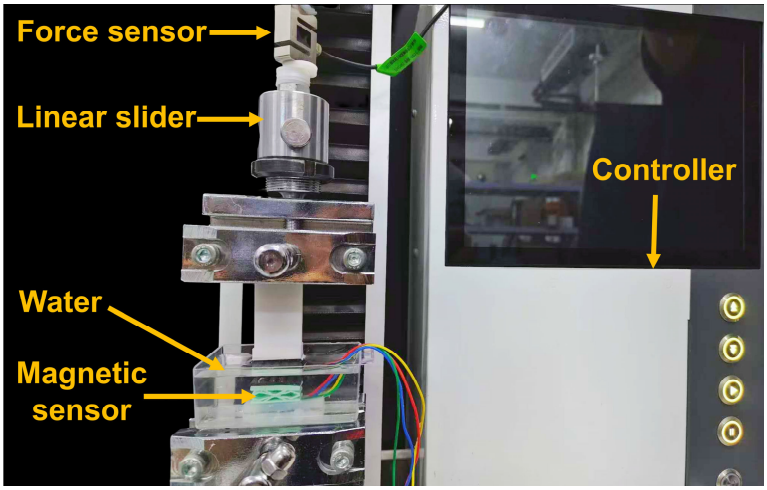

Figure S5. Schematic showing the mechanical testing specimens and the corresponding experimental setup used in this study.

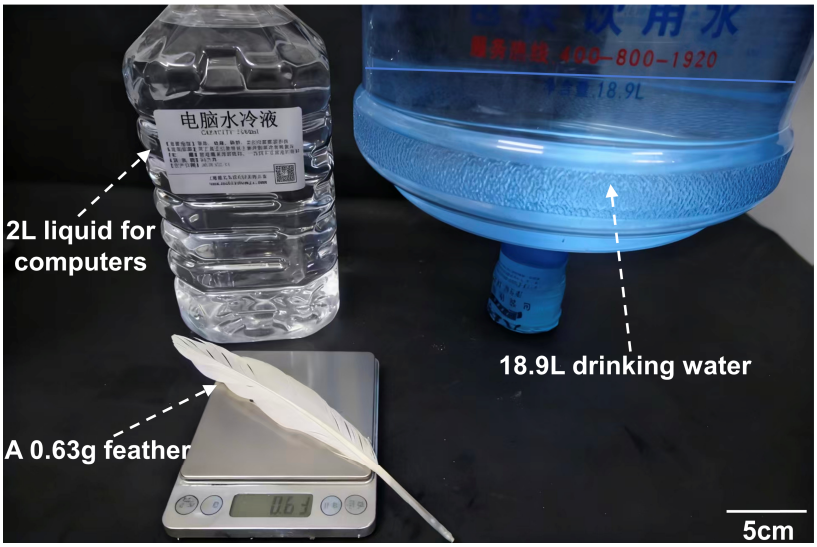

Figure S6. A set of objects used for testing the measurement range of the tactile sensor, featuring masses of 0.63 g (a feather), 18.9 L (drinking water), and 2 L (liquid for computers).

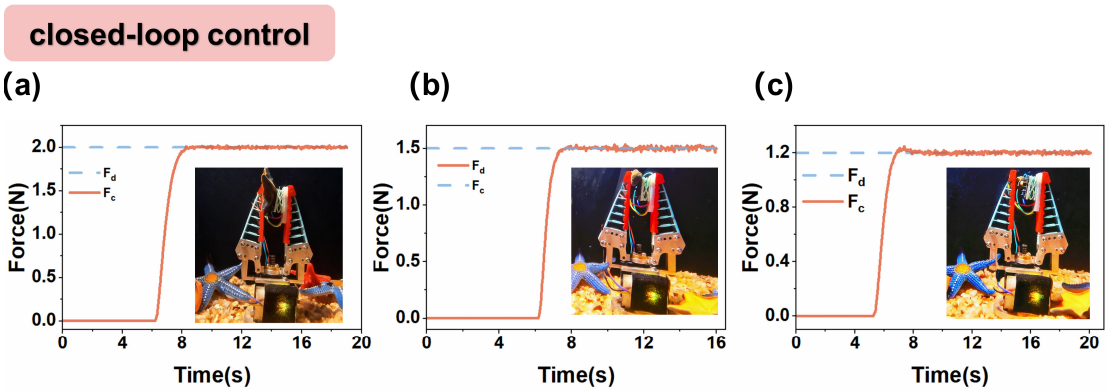

Figure S7. Validation of closed-loop control and non-damaging grasping based on tactile feedback. (a) Process of non-damaging grasping for a sea star. (b) Process of non-damaging grasping for a sea cucumber. (c) Process of non-damaging grasping for a sea snail.

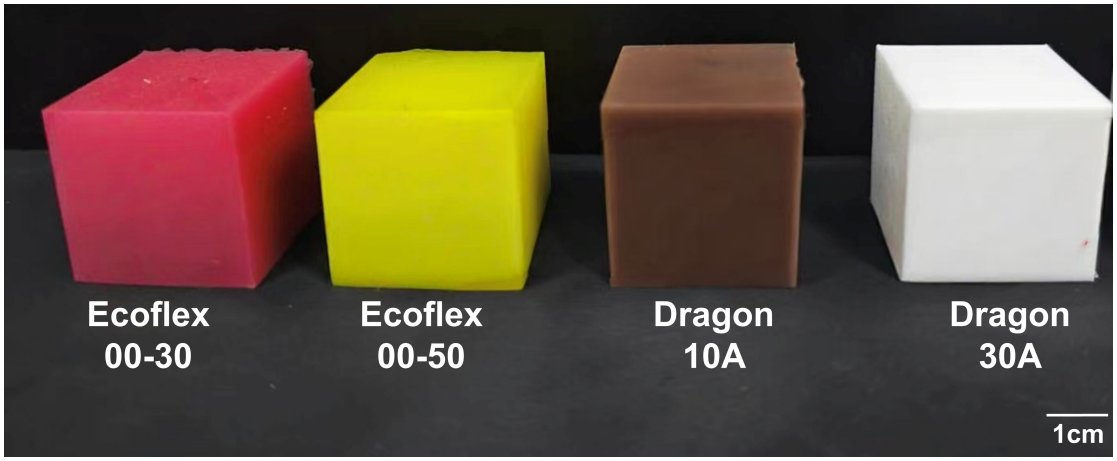

Figure S8. Four material samples with different hardness levels used for gripping identification.

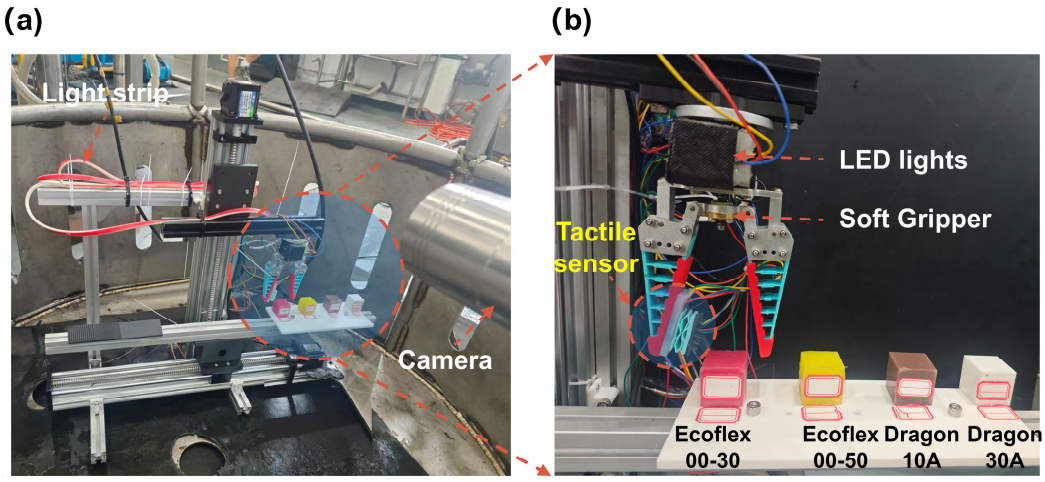

Figure S9. Schematic of the experiment for object hardness identification using the tactile sensor. (a) The grasping system mounted on an enclosure structure. (b) A soft gripper integrated with the deep-sea tactile sensor, along with four silicone material samples of different Shore hardness, employed to validate the sensor's capability for material hardness discrimination.

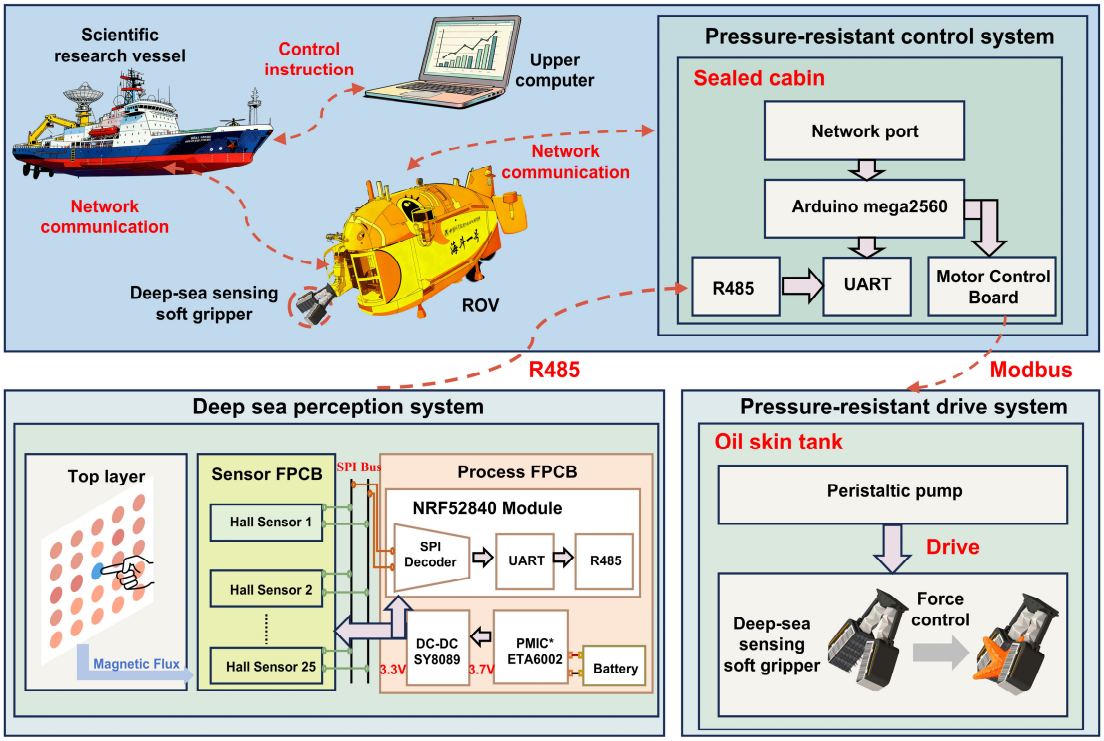

Figure S10. Hierarchical control architecture of the deep-sea tactile soft grasping system. The system employs a three-layer structure—surface (research vessel), carrier (ROV platform), and end-effector (operational gripper)—to enable remote command and data interaction. The terminal system consists of three core modules: (1) The actuation module (including a peristaltic pump and a pressure-compensated oil bladder), responsible for generating and regulating the grasping force; (2) The control module, which coordinates all subsystems via an RS-485 bus and enables real-time communication with the ROV; (3) The sensing module (integrating a 5×5 Hall sensor array), whose signals are acquired through a flexible printed circuit, read by an NRF52840 module, and transmitted back to the control module via RS-485, thereby forming a tactile feedback loop. This architecture achieves full-link integration from surface command to deep-sea force control, supporting a "perception-decision-execution" closed loop for adaptive grasping in deep-sea environments.

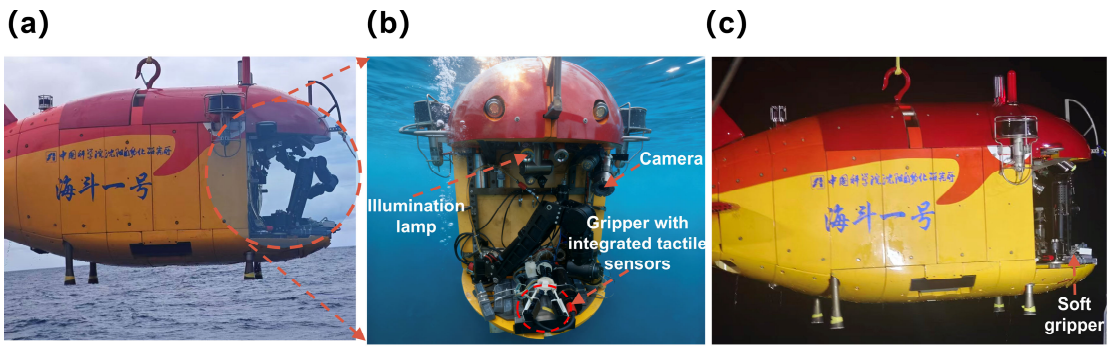

Figure S11. In-situ sea trial validation of the deep-sea tactile perception system deployed on the "Haidou-1" ROV. (a) The integrated soft gripper with tactile sensors being prepared for deployment on the mother ship's deck. (b) The system descending with the ROV to a maximum depth of 2284.7 meters. (c) The system safely retrieved back on deck alongside the ROV upon completion of the operation.

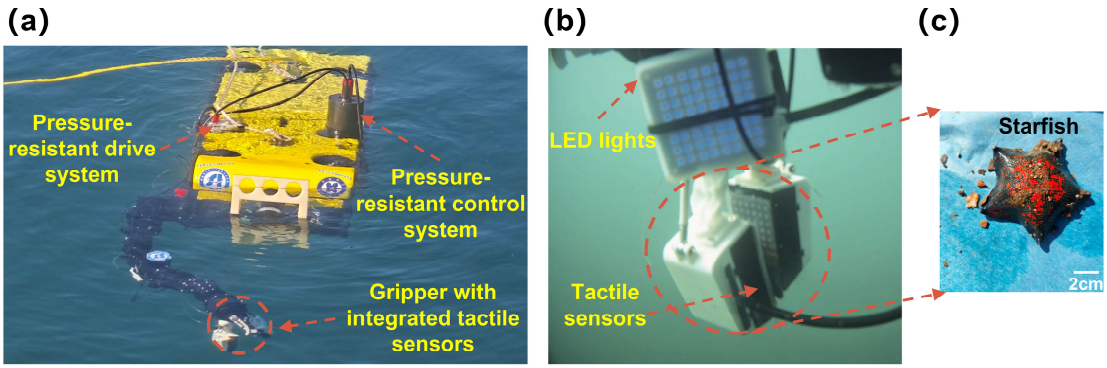

Figure S12. Operational workflow of the deep-sea adaptive grasping system deployed on the ROV platform. (a) Overall deployment scenario showing the integrated deep-sea operation system, comprising perception, actuation, and control units, during descent. (b) In the underwater environment, the system performs adaptive force-closed-loop grasping of a sea star based on real-time tactile feedback. (c) Successfully retrieved sea star sample, demonstrating the system's capability for non-damaging manipulation of fragile deep-sea organisms.

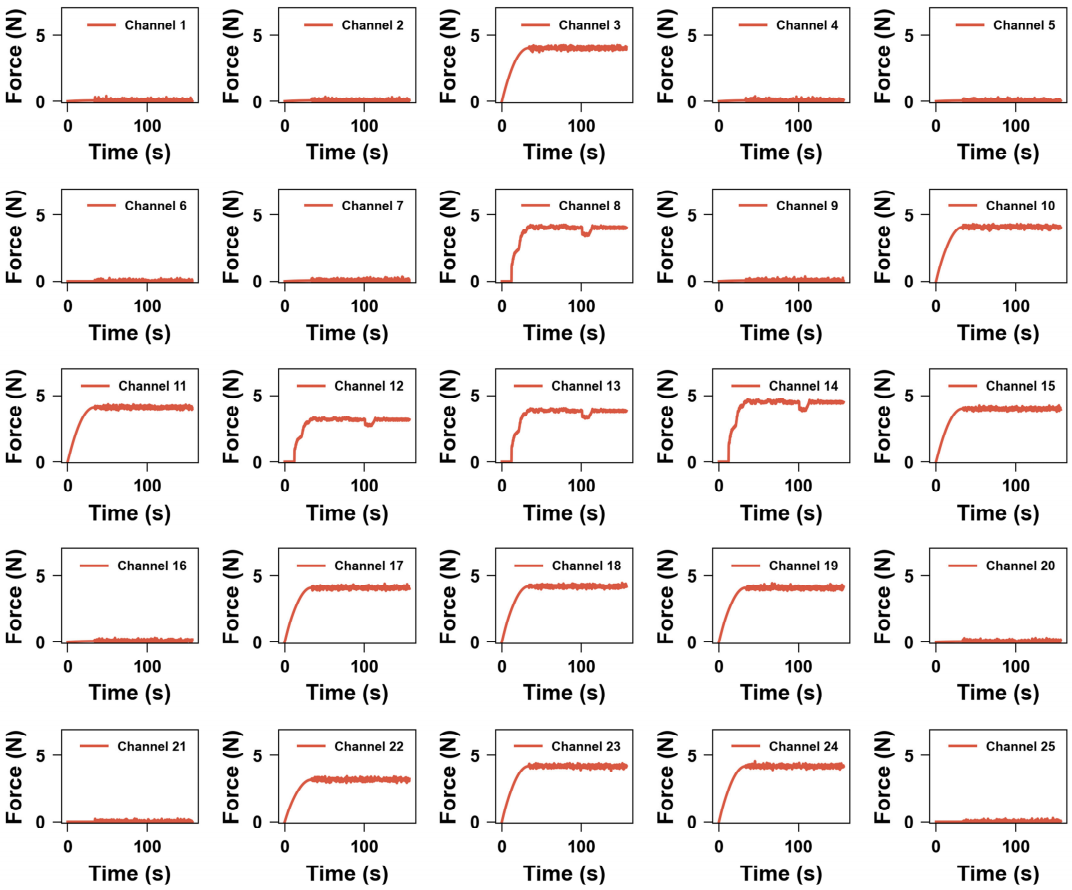

Figure S13. Time sequence diagram of 25-channel tactile forces during the sea star grasping process.

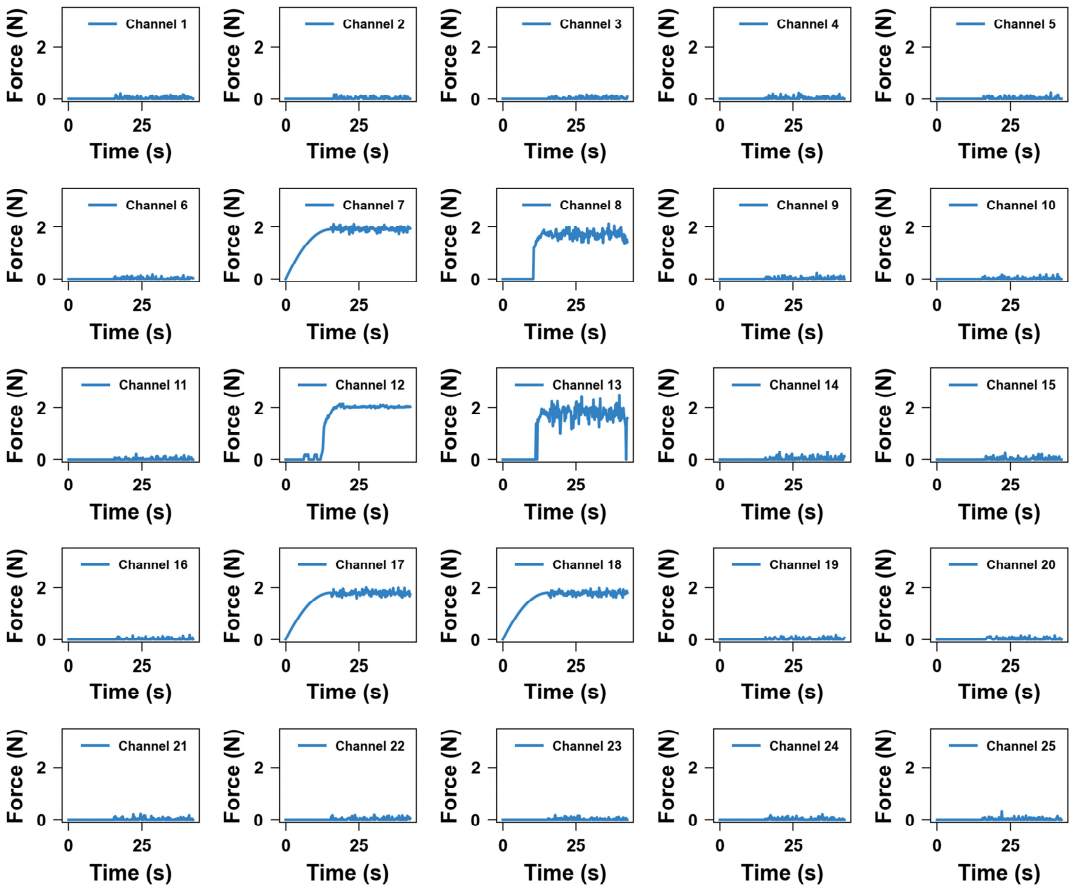

Figure S14. Time sequence diagram of 25-channel tactile forces during the sea cucumber grasping process.

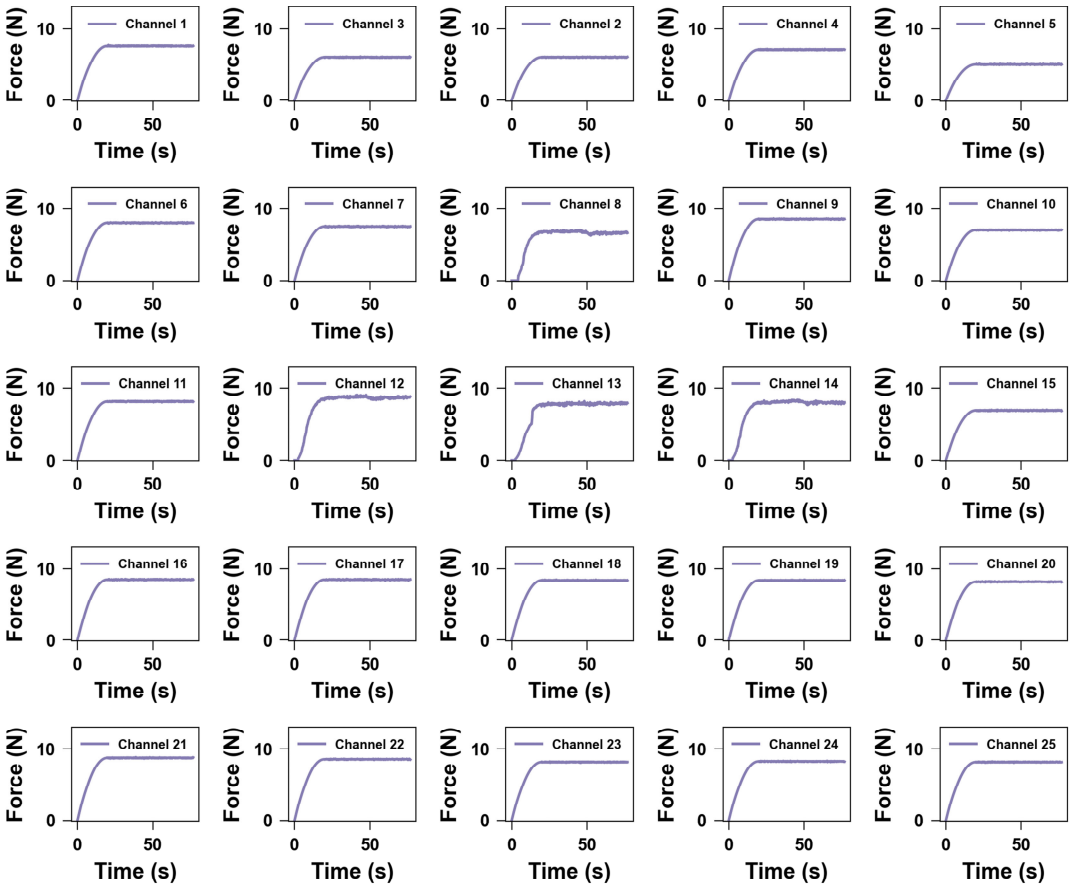

Figure S15. Time sequence diagram of 25-channel tactile forces during the sea snail grasping process.

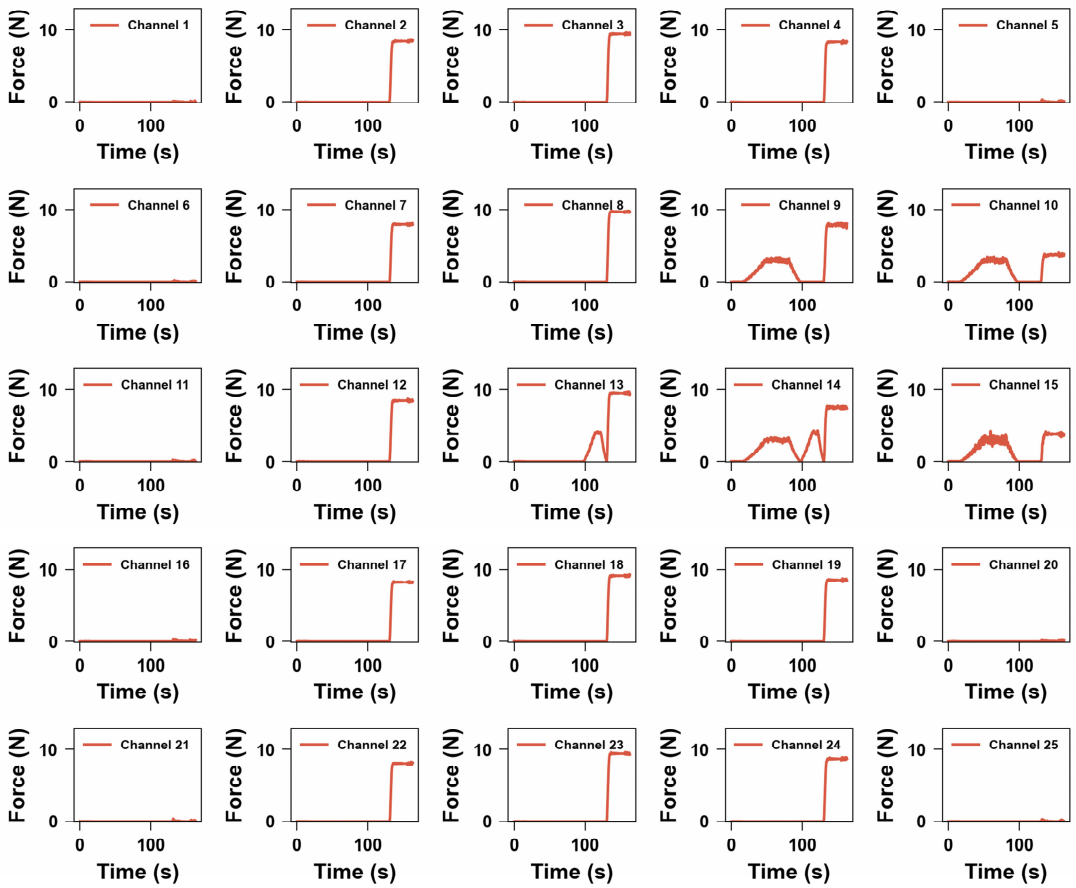

Figure S16. Time sequence diagram of 25-channel contact forces during the tactile-feedback-based collaborative sampling process.

References

1. Wang, Q., et al., *Multi-Hierarchically Porous SWNTs-TPU/C-WPU Composite Film for Underwater Self-Powered Multi-Modal Tactile Information Sensing.* Advanced Functional Materials, 2025.
2. Wu, J., et al., *A deep-sea pressure sensor capable of sensing small gripping forces without coupling.* Science China Materials, 2025.
3. Zhang, Z., et al., *Waterproof and Flexible Aquatic Tactile Sensor with Interlocked Ripple Structures for Broad Range Force Sensing.* Advanced Materials Technologies, 2023. **9**(2).
4. Xiang, F., et al., *Highly Sensitive Aquatic Iontronic-Based Tri-Axis Force Sensor Array for Underwater Robotic Gripping.* IEEE Transactions on Instrumentation and Measurement, 2025. **74**: p. 1–10.
5. Liu, S., et al., *Tactile Sensing for Soft Robotic Manipulators in 50 MPa Hydrostatic Pressure Environments.* Advanced Intelligent Systems, 2023. **5**(12).
6. Wang, Q., et al., *Self-Powered Underwater Pressing and Position Sensing and Autonomous Object Grasping with a Porous Thermoplastic Polyurethane Film Sensor.* Advanced Functional Materials, 2024. **34**(28).
7. Zuo, Z., et al., *A Deep-Sea Sensorized Soft Gripper With Force Estimation and Interactive Capabilities.* IEEE/ASME Transactions on Mechatronics, 2025: p. 1–11.
8. Liu, X., et al., *Fish-Like Dual-Bubbling Nanostructured Membranes-Based Actuation System for Enhanced Underwater Sensing.* Advanced Functional Materials, 2025.